Nanoscale Advances

ROYAL SOCIETY OF CHEMISTRY

PAPER

View Article Online
View Journal | View Issue

Cite this: *Nanoscale Adv.*, 2025, **7**, 1143

Morphology controlled Cu_3BiS_3 nanostructures: superior electrocatalytic sensing of organic nitro compounds†

Manzoor Ahmad Pandit,‡[ab] Dasari Sai Hemanth Kumar, ‡[b] Mohan Varkolu [bc] and Krishnamurthi Muralidharan *[b]

Addressing the pressing need to develop affordable and efficient catalysts is essential. In this study, we successfully synthesized Cu_3BiS_3 nanostructures with a modified morphology using three different nitrogen bases: DBN, DBU, and DABCO *via* a hydrothermal technique. These nanostructures were used for the electrochemical detection of organic nitro groups, a previously unexplored application for this material. We conducted a thorough characterization of the Cu_3BiS_3 nanostructures using various analytical and spectroscopic methods, including PXRD, FESEM, TEM, XPS, UV-vis, and BET, ensuring the reliability of our results. We then investigated their performance in the electrochemical detection of 4-dinitrophenol (4-NP) and 2,4-dinitrophenol (2,4-DNP) using a modified glassy carbon (GC) electrode. The Cu_3BiS_3 material produced using DABCO exhibited better sensitivity towards 4-NP detection, with a low limit of detection (LOD) of 0.50 μM compared to the ones synthesized using DBN and DBU. Furthermore, the synthesized materials demonstrated the ability to detect their structural analogue, 2,4-DNP. The distinctive hierarchical nanostructures attained in Cu_3BiS_3 highlight the benefits of developing such catalysts and the impact of nitrogenous bases in defining the morphology of the materials with enhanced catalytic activities.

Received 21st October 2024
Accepted 20th December 2024

DOI: 10.1039/d4na00871e

rsc.li/nanoscale-advances

1 Introduction

With the rapid progress in science and technology and the widespread growth of industries, the demand for fuels and the use of chemicals has increased significantly.[1–7] This development has resulted in a surge in CO_2 emissions, toxic chemicals, and other greenhouse gases, leading to environmental devastation. Industries release excessive phenolic compounds into the ecosystem, with nitrophenol being one of the most hazardous. Many industries use nitrophenols to produce various chemicals, such as dyes, medicines, and pesticides.[8,9] These nitrophenols are carcinogenic, poisonous, inhibitory, and resistant to biological degradation. In particular, 4-nitrophenol (4-NP) and 2,4-dinitrophenol (2,4-DNP) are highly toxic and cause environmental and biological harm.[10,11] Even in small amounts, 4-NP affects organs such as the brain and kidneys.[12–15] Due to its strong chemical stability and microbial degradation resistance, purifying water bodies contaminated with 4-NP is complicated. Therefore, it is designated as a toxic contaminant worldwide.

The techniques used to detect nitrophenols, such as UV-visible spectroscopy and HPLC, are time-consuming since they require the transfer of samples to the instruments. The literature describes alternative methods like flow injection reflectors, high-performance capillary zone electrophoresis, and enzyme-mediated immune sorbent assays to detect 4-NP. However, their high post-treatment costs and rigorous testing conditions hinder their widespread adoption.[16] As a result, electrochemical detection using nanomaterial-based sensors has emerged as a practical approach due to its rapid response, ease of operation, high sensitivity, cost-effectiveness, and eco-friendliness.[17] For example, Nurul *et al.* successfully synthesized silver nanoparticles supported on graphene oxide to detect 4-NP, achieving a limit of detection (LOD) of 1.2 nM.[8] Dhanasekaran *et al.* reported the synthesis of silver nanoparticles doped on Co–Al layered double hydroxides protected by poly(*o*-phenylenediamine) as electrocatalysts, which exhibited a LOD of 63 nM and 50 nM for detecting 4-NP and 2,4-DNP, respectively, through electrochemical methods.[18] Considering the significant LOD of these materials for 4-NP detection, it is imperative to develop improved catalysts for both the detection and degradation of 4-NP and its similar compounds.

[a]*Materials Genome Institute, Shanghai University, Shanghai 200444, China*
[b]*School of Chemistry, University of Hyderabad, Hyderabad 500046, Telangana, India. E-mail: murali@uohyd.ac.in*
[c]*Department of Chemistry, College of Engineering, Koneru Lakshmaiah Education Foundation, RVS Nagar, Azziz Nagar (PO), Moinabad Road, Hyderabad 500075, Telangana, India*

† Electronic supplementary information (ESI) available. See DOI: https://doi.org/10.1039/d4na00871e

‡ Both the authors contributed equally.

Transition metal chalcogenides have garnered significant attention due to their exceptional physical, chemical, and electrochemical properties. The presence of vacant d-orbitals in transition metals enables the formation of chalcogenides with diverse compositions and stoichiometry, including binary, ternary, and quaternary structures.[19] These nanostructures exhibit unique characteristics, such as varying bandgaps, excellent electrical conductivity, and smooth charge carrier transfer. Owing to these versatile features, transition metal chalcogenides are used in energy conversion and storage devices, thermoelectric systems, electro-photo catalysis, energy harvesting materials, and hydrogen generation.[20–27]

Copper-containing semiconductors prepared from abundant and environmentally safe elements have shown great promise as photoelectrocatalysts. Nanostructured materials like Cu_2SnS_3, Cu_2ZnSnS_4, Cu_2FeSnS_4, and Cu_2BaSnS_4 have been found to be excellent candidates for photoelectrocatalytic water splitting due to their favorable bandgap (1.2–1.5 eV) and high absorptivity coefficients.[28] In particular, the wittichenite crystal phase of Cu_3BiS_3 is considered highly suitable for photovoltaic absorption, boasting a high absorptivity coefficient of $\sim$104 cm^{-1} and an appropriate band gap of $\sim$1.5–1.7 eV.[29,30] For instance, Jiajia *et al.* synthesized a Cu_3BiS_3 nanorods/TiO_2 heterostructure using a simple solution dip-coating technique, which displayed stronger absorption in the visible region compared to pure Cu_3BiS_3 and pure TiO_2.[31] When utilized for the photoelectrochemical hydrogen evolution reaction, this material outperformed pure Cu_3BiS_3 nanorods. While the Cu_3BiS_3 nanostructure exhibits impressive properties, its capabilities in CO_2 and N_2 reduction, as well as its potential for detection/sensing applications, have not been extensively explored and warrant further investigation.

We have developed a hydrothermal process to prepare the wittichenite phase of Cu_3BiS_3 in various morphologies using three different organic nitrogenous bases: DBU, DABCO and DBN. These bases served as ligands or stabilizers to regulate the product's morphology. In this study, for the first time, we present Cu_3BiS_3 in three different forms – spheres, rods, and worm-like structures for electrochemical 4-NP detection and its analogs (2,4-DNP). These catalysts exhibited remarkable optical and charge transport properties and possess large specific surface areas, as demonstrated by their excellent electrochemical activities.

2 Experimental

2.1 Materials

Cuprous nitrate ($Cu(NO_3)_2 \cdot 5H_2O$), $Bi(NO_3)_2 \cdot 5H_2O$, thiourea, DBU, DABCO, DBN, ethanol, water, and ethylene glycol were obtained from Sigma-Aldrich. The chemicals were high purity; no other second purification step was required.

2.2 Synthesis of Cu_3BiS_3

Step-i: in a typical synthesis, a solution was created by mixing ethanol (32 ml), water (2 ml), and ethylene glycol (22 ml) in a round-bottom flask. The precursors of $Cu(NO_3)_2 \cdot 5H_2O$ (200 mg, 1.07 mmol), $Bi(NO_3)_2 \cdot 5H_2O$ (110 mg, 0.35 mmol), and DBU (50 μL, 0.35 mmol) were simultaneously added to the solution. The resulting mixture was then transferred to a hydrothermal bomb and stirred for 24 hours. Subsequently, the reaction temperature was set at 170 °C for 2 hours and then cooled to room temperature. The resulting mixture was washed with distilled water multiple times to obtain CuBi precursor. It was dried in a vacuum oven to remove any moisture.

Step-ii: the dried material (CuBi precursor) was dispersed again in 55 ml of distilled water and stirred for 30 minutes, followed by the addition of thiourea (81 mg, 1.07 mmol). The mixture was left for 6 hours at 160 °C in a hydrothermal bomb. After the allotted time, the reaction mixture was allowed to cool to room temperature. The resulting black materials were washed with ethanol and water several times and then dried in an oven at 60 °C for 24 hours.

The similar reactions were performed in the presence of DBN (42 μL, 0.35 mmol) and DABCO (59 mg, 0.35 mmol) separately. The final materials obtained were labeled as Cu_3BiS_3-DBU, Cu_3BiS_3-DBN, and Cu_3BiS_3-DABCO.

2.3 Characterization and instrumentations

The crystal structure predictions of Cu_3BiS_3 were determined using powder X-ray diffraction (PXRD) with a Bruker D8 X-ray diffractometer equipped with a Cu-Kα radiation source (λ = 0.15406 nm). Surface analyses were carried out using field-emission scanning electron microscopy (FESEM) with an Ultra 55 Carl Zeiss instrument operating at 10 kV, as well as transmission electron microscopy (TEM) with an FEI Technai G2 20 STEM with a 200 kV acceleration voltage. Optical properties, such as absorption spectrum and band gap, were examined using a JASCO-V770 UV/Vis spectrometer. Surface area and pore size analysis were conducted based on adsorption–desorption isotherms using Quantachrome instruments. The elemental composition and oxidation states were also analyzed *via* X-ray photoelectron spectroscopy (XPS) using a Thermal Scientific Escalab 250Xi spectrometer with Al-Kα radiation.

2.4 Electrochemical measurements

The prepared materials were evaluated for the electrochemical reduction of 4-nitrophenol (4-NP) and 2,4-dinitrophenol (2,4-DNP) using CHI 6612E (Shanghai Chenhua Instrument Co., China) electrochemical workstation in a three-electrode set up. The platinum electrode served as a counter electrode, silver/silver chloride (3.5 M KCl) as the reference electrode, and the electrocatalyst-modified glassy carbon electrode (GCE) as the working electrode. The catalyst was prepared by taking 2 mg of either Cu_3BiS_3-DBU, Cu_3BiS_3-DBN, or Cu_3BiS_3-DABCO in a mixture of water and isopropanol followed by addition of 30 μl of Nafion binder. The prepared slurry of catalyst was coated on the surface of pre-cleaned GCE. The 0.1 M phosphate buffer solution (PBS) was used as supporting electrolyte at different pH. Varying amounts of 4-NP and 2,4-DNP were added into the buffer solution while performing sensing activity.

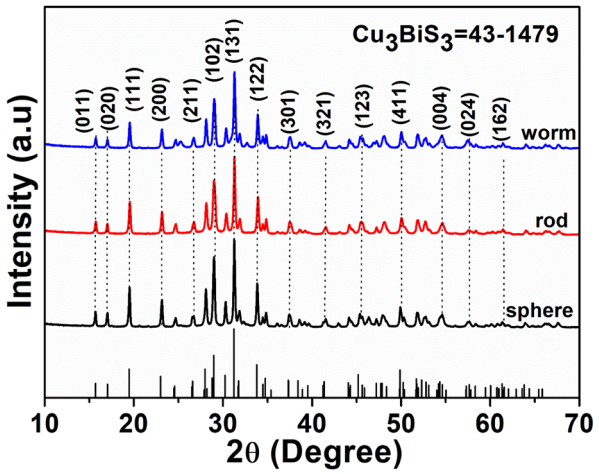

Fig. 1 The PXRD patterns of Cu_3BiS_3 (JCPDS 43-1479) obtained using DBU (spheres), DBN (worms) and DABCO (rods).

3. Results and discussion

3.1 Synthesis and characterization of Cu_3BiS_3 nanostructures

A hydrothermal method was employed to produce Cu_3BiS_3 nanomaterials with diverse morphologies using three different organic bases (DBN, DBU, and DABCO). The crystal structure and phase purity of the prepared Cu_3BiS_3 were analyzed using Powder X-ray diffraction (PXRD) (Fig. 1), revealing that all peaks in the three PXRDs can be attributed to the orthorhombic phase of Cu_3BiS_3 (JCPDS 00-043-1479, a = 7.696 Å; b = 10.38 Å, c = 6.711 Å). The diffraction peaks at 2θ value of 15.74°, 17.09°, 19.53°, 23.15°, 24.70°, 26.74°, 28.10°, 29.00°, 30.31°, 31.31°, 33.88°, 34.87°, 36.07°, 41.51°, 43.04°, 44.17°, 45.34°, 46.38°, 48.01°, 49.91°, 51.83°, 52.77°, 54.55° and 57.61° belong to (110), (020), (111), (200), (210), (201), (211), (031/102), (112), (131/102), (122), (230), (301), (321), (113), (241), (312), (331), (410), (133/340), (251), (060), (430) and (323/342) diffraction planes. The most intense sharp peak at 31.2° corroborates the (131) crystal facet of the material, consistent with JCPDS card data 43-1479.[32] No diffraction peaks corresponding to other phases of Cu_3BiS_3 were detected, underscoring the phase purity of Cu_3BiS_3.

The XPS analyses have verified the existence of specific elements and their chemical states in the produced materials. Fig. 2 displays the survey spectrum of Cu_3BiS_3 hierarchical structures, confirming the presence of Cu, Bi, and S elements. Furthermore, in Fig. 2b, the notable intense peaks at 936.4 eV and 956.7 eV binding energies closely resemble the Cu $2p_{3/2}$ and Cu $2p_{1/2}$ peaks of Cu_3BiS_3. Additionally, Fig. 2c illustrates the binding energies of the bismuth 4f doublet at 162.1 eV and 168.5 eV, corresponding to the Bi $4f_{7/2}$ and Bi $4f_{5/2}$. The spin-orbit splitting value of Cu 2p and Bi 4f is calculated to be 19.7 eV (Cu^+) and 5.3 eV (Bi^{3+}). The S 2p peak is observed at the

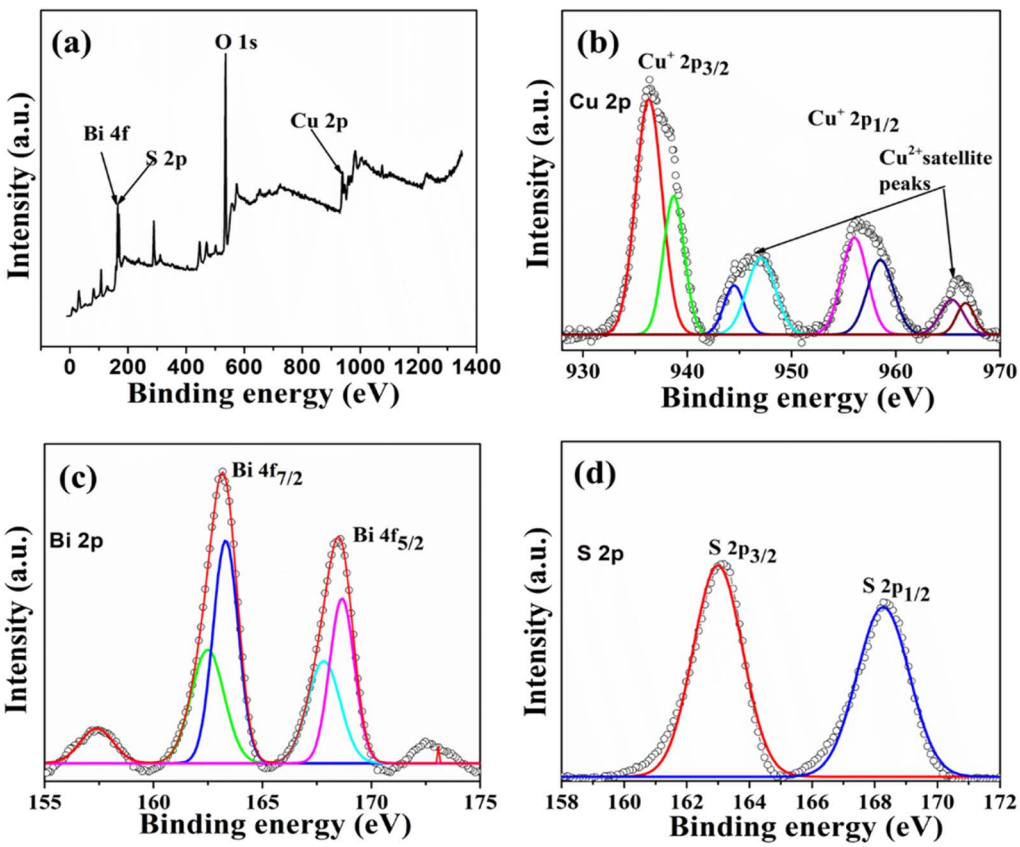

Fig. 2 The XPS spectra of Cu_3BiS_3 nanostructures (a) survey spectrum showing the presence of all the required elements. (b) XPS spectra of Cu 2p (c) XPS spectrum of Bi 4f and (d) XPS spectrum of S 2p.

binding energy of 163.1 eV, consistent with existing literature reports. Consequently, the XPS spectra of Cu_3BiS_3 nanostructures validate the presence of Cu^+, Bi^{3+}, and S^{2-} chemical states within the obtained Cu_3BiS_3.[28]

3.2 Morphology and surface area of Cu_3BiS_3 nanostructures

The examination of Cu_3BiS_3 nanomaterials using FESEM revealed variations in the surface morphology of three samples produced in reactions in the presence of three different bases (Fig. 3). Cu_3BiS_3-DBU samples displayed a spherical morphology, Cu_3BiS_3-DABCO showed a rod-like surface, and Cu_3BiS_3-DBN exhibited a worm-like morphology (Fig. 3a–c). The morphological results clearly indicate that the organic basis played a well definite role in architecting the surface of nanocrystals, which have great impact on the catalytic activities of achieved structures. The high magnification FESEM images representing individual sphere, rod, and worms are shown in Fig. S1.† The average particle size of Cu_3BiS_3 nanostructures is calculated as shown in Fig. S2a–c.† Additionally, TEM analysis confirmed the spherical morphology of Cu_3BiS_3-DBU with an average diameter of 101.89 nm, the rod-like topography of Cu_3BiS_3-DABCO with an average length of 13.84 nm and an average width of 21.19 nm, and the worm-like morphology of Cu_3BiS_3-DBN with an overall size of 97.85 nm (Fig. 3d–f). The EDAS (Fig. S3†) additionally reveals that all the elements were equally distributed within the Cu_3BiS_3 nanostructures. Furthermore, the high-resolution TEM micrographs of the synthesized materials exhibited close d-spacing with their corresponding PXRD. The distances of 0.28 nm between lattice fringes were consistent with the (131) crystal planes for the sphere-shaped material. Similarly, interplanar spacings of 0.28 nm corresponded to (131) plane for the rod-shaped material, while the spacing of 0.28 nm aligned with the (131) crystal facet of the worm-shaped material. The corresponding SAED patterns of synthesized Cu_3BiS_3 nanomaterials are shown in Fig. S1d–f.† The bright spots in SAED reveals the high crystalline nature of Cu_3BiS_3 nanomaterials which is in good agreement with the PXRD values.

Besides surface morphology, the exceptional catalytic activities of nanostructured materials can also largely be attributed to their specific surface area. In this study, we analyzed the nitrogen adsorption–desorption BET isotherms of Cu_3BiS_3 materials (refer to Fig. 4). The specific surface areas of the three Cu_3BiS_3 nanostructures exhibiting spherical, rod-like, and worm-like morphologies were 19.570 $m^2\ g^{-1}$, 22.723 $m^2\ g^{-1}$, and 33.676 $m^2\ g^{-1}$, respectively. Additionally, the pore size distribution of Cu_3BiS_3 nanostructures (refer to Fig. S4†) fell within the 10–15 nm range, indicating a mesoporous structure.

The solid-state UV-visible diffuse reflectance spectra at room temperature examined the optical properties of these materials

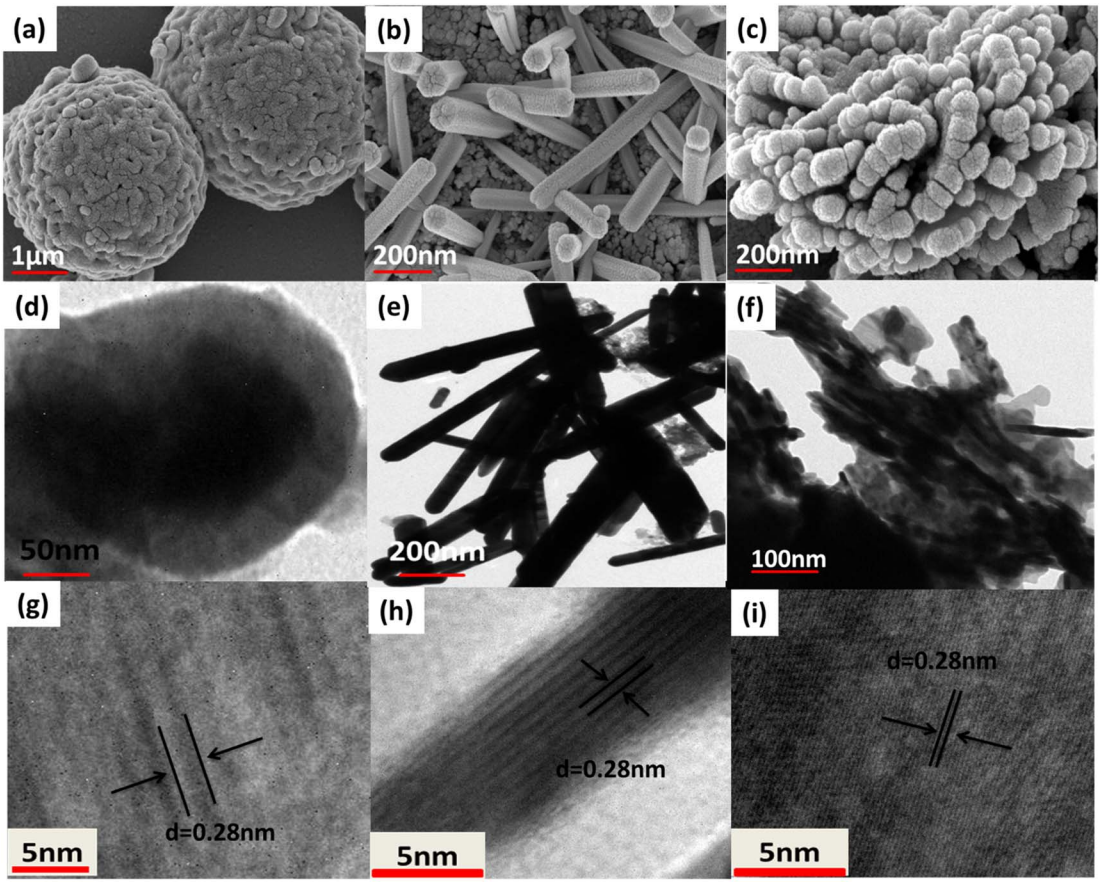

Fig. 3 FESEM images: (a) spheres of Cu_3BiS_3-DBU, (b) rods of Cu_3BiS_3-DABCO, (c) worm-like morphology of Cu_3BiS_3-DBN. TEM (d) spheres, (e) rods, (f) worms of Cu_3BiS_3 and their respective HRTEM images (g–i) with d-spacing.

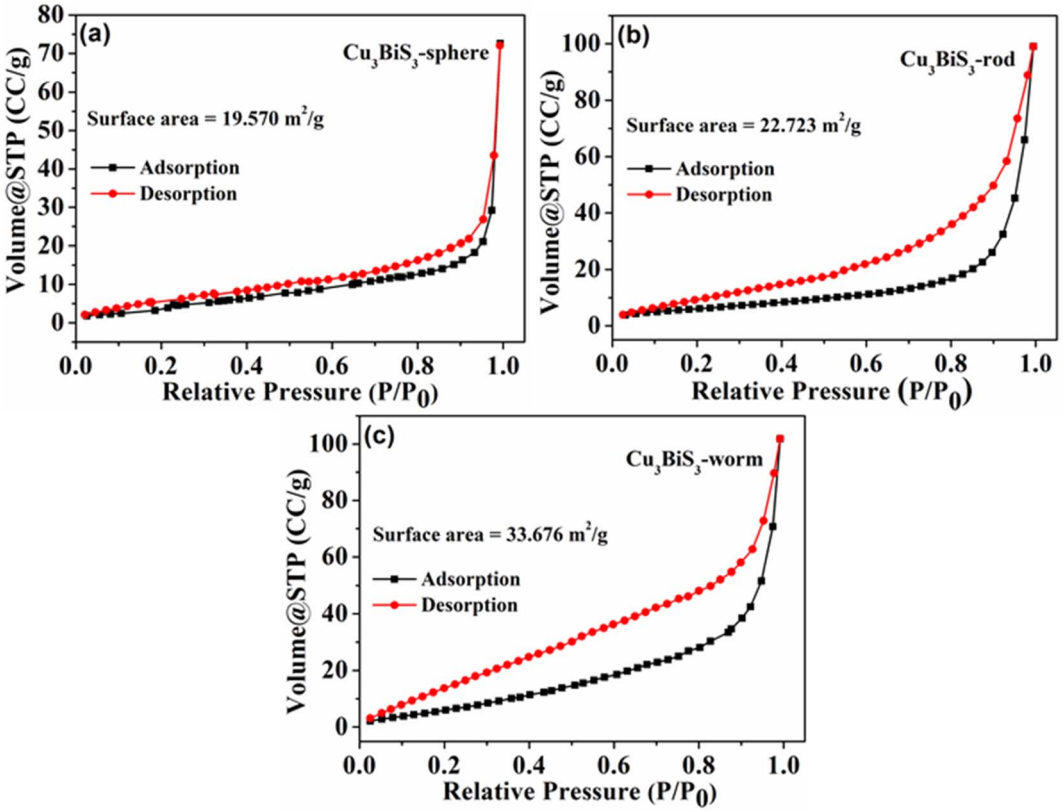

Fig. 4 The nitrogen adsorption–desorption isotherms of Cu_3BiS_3 nanostructures (a) spheres (b) rods (c) worms.

in the range of 200 to 1200 nm. Analysis of the spectra (Fig. S5a†) revealed three broad peaks in the absorption spectrum of the synthesized Cu_3BiS_3 materials, spanning 400 to 800 nm. The optical band gap of Cu_3BiS_3 materials (Cu_3BiS_3-DBU, Cu_3BiS_3-DBN, and Cu_3BiS_3-DABCO) (Fig. S5b†) was determined from the Tauc plot are found to be in the range of 0.45 to 0.90 eV. These measured band gap values are relatively low compared to those previously reported in the literature, suggesting that particle size may have a significant effect.

3.3. Electrochemical detection of 4-NP and 2,4-DNP

The catalyst's electrochemical behavior was explored in a solution containing 100 μM 4-NP in 0.1 M PBS. The resulting cyclic voltammograms (CV) of Cu_3BiS_3 at different pH levels (5–9) are shown in Fig. 5. As expected, the CV results of the plain GCE exhibited a low reduction current. The obtained CV curves of Cu_3BiS_3-DBU and Cu_3BiS_3-DABCO materials with sphere and rod morphology showed poorer current responses (Fig. 5a and b) compared to Cu_3BiS_3-DBN with a worm-like morphology (Fig. 5c). The higher reduction current of Cu_3BiS_3-DBN is primarily attributed to its larger surface area, presence of a greater number of active sites, and hierarchical morphological structure. The activity of Cu_3BiS_3 towards 4-NP was primarily identified by adding 4-NP to 0.1 M PBS solution at pH 6. It was observed that (Fig. S6a–c†) the current was increasing with the addition of 4-NP, which clearly indicated the sensing activity of Cu_3BiS_3 materials.

The pH of the medium significantly influenced the electrochemical detection of 4-NP due to the involvement of phenolic hydroxyl groups in proton transfer reactions, leading to the formation of quinones.[33,34] The current plots obtained at different pH levels (5 to 9) for all three materials (Fig. 5d–f) showed the maximum reduction current achieved in the case of Cu_3BiS_3-DBN (worm-like). The pH studies revealed that as the pH increased from 5 to 9, the cathodic peak potential of 4-NP consistently shifted to the negative side. The peak current (I_{pc}) of 4-NP was identified to be higher at pH 6.0. Therefore, for further evaluation of the materials' sensing/detection performance, pH 6.0 was considered the optimal pH in this study.

We conducted a study to assess the impact of 4-NP concentrations on the reduction current at 0.1 M PBS pH 6. We plotted the effect of increasing 4-NP concentrations from 10 μM to 100 μM on the CV (Fig. 6a–c). Our findings indicated that the higher concentration of 4-NP led to a more pronounced intensity of the reduction peak in worms (Fig. 6c) than in sphere and rod morphologies (Fig. 6a and b). Moreover, when we correlated the plots of reduction peak current with the concentration of 4-NP, we observed linear fits, as depicted in Fig. 6d–f. This observation suggests that the increase in concentration had a linear effect on the detection of 4-NP by the synthesized materials, with the maximum limit observed for Cu_3BiS_3-DBN worms.

Furthermore, in order to explore the changing aspects of the electrode reaction, we studied the CV curves of Cu_3BiS_3 at different scan rates while maintaining the 4-NP concentration

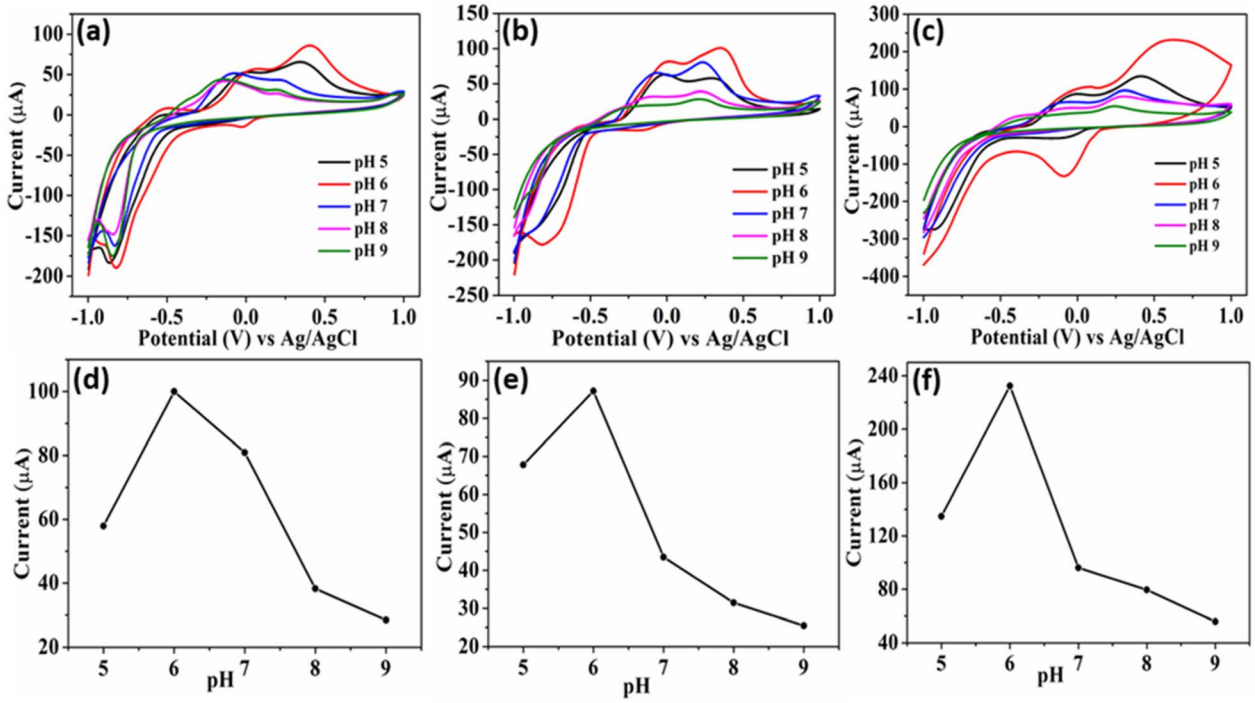

Fig. 5 CV of Cu_3BiS_3 for 100 μM 4-NP at different 0.1 M PBS pH (5–9) (a) Cu_3BiS_3-sphere, (b) Cu_3BiS_3-rod, and (c) Cu_3BiS_3-worm. (d–f) The corresponding plots of current *vs.* different pH.

constant. The graphs in Fig. 6(g–i) illustrate that as the scan rates increased (20–120 mV s^{-1}) at a constant 100 μM concentration of 4-NP (pH-6) within a potential window of −1.0 to 1.0 V, there was an increase in the reduction peak current. This enhancement was most noticeable in the Cu_3BiS_3-DBN worms compared to the other two morphologies, Cu_3BiS_3-DBU spheres and Cu_3BiS_3-DABCO rods. This enhanced activity of Cu_3BiS_3-DBN worms was further supported by the graphs obtained by plotting the square root of scan rates against peak currents (Fig. S6d–f†). The linear trend line indicates a sharp increase in current, possibly due to the diffusion-controlled process.

For further exploration of the 4-NP sensing, the limit of detection (LOD), limit of quantification (LOQ) and sensitivity of the three morphologically different Cu_3BiS_3 materials were studied. The LOD were calculated by the equation as:[35]

$$\mathrm{LOD} = 3 \times \sigma/S$$

$$\mathrm{LOQ} = 10 \times \sigma/S$$

where σ is the standard deviation of the blank sample and S is the slope of the calibration curve. By using this equation, the LOD was determined to be 0.19, 0.13, 0.10 μM for Cu_3BiS_3-S, Cu_3BiS_3-R, and Cu_3BiS_3-W respectively. In Table 1 we have reported the comparison of 4-NP electrochemical detection by the as synthesized Cu_3BiS_3 nanomaterials with different morphologies. From the results, it is observed that our approach of synthesizing materials has achieved a lower value of LOD, which may be credited to the high specific surface area of the synthesized materials and the resilient contact between the improved electrode surface and analytes. Therefore, it is clear that the Cu_3BiS_3-DBN modified electrode requires the low potential for detection of 4-NP at micromolar levels.

Electrochemical impedance spectroscopy (EIS) is a crucial tool for evaluating electrochemical behaviour. The electrical hysteresis characteristics of Cu_3BiS_3 and bare glassy carbon electrode (GCE) were investigated using EIS in a 5 mM $K_3[Fe(CN)_6]$ solution. The loaded electrode created an arc with a lesser radius than the unloaded electrode in EIS (Fig. 7h). This result indicated that the Cu_3BiS_3-DBN nanomaterial effectively reduces the charge transfer resistance of the GCE surface, leading to improved electron conduction efficiency compared to the unloaded electrode. The presence of Cu_3BiS_3-DBN with a worm-like morphology significantly alters the electrical properties of the GCE surface, making it a promising EIS sensor for detecting cells, bacteria, and biomarkers. Conversely, Cu_3BiS_3 with spherical and rod-like morphologies do not exhibit similar effectiveness. The electroactive surface area was examined using CV in 0.1 M KCl solution containing 5 mM $K_3[Fe(CN)_6]$, as shown in Fig. 7g. The enhanced peak current observed in the Cu_3BiS_3-DBN with a worm-like morphology indicates an increased active surface area, which is attributed to the improvement in the redox reaction of $Fe(CN)_6^{3-/4-}$. These results suggest that Cu_3BiS_3-DBN exhibits superior electron transfer capability compared to Cu_3BiS_3-DABCO and Cu_3BiS_3-DBU.

An analogous electrochemical phenomenon was observed in detecting 2,4-DNP in the presence of Cu_3BiS_3 nanocatalysts. Various studies were conducted to analyze the impact of different parameters, such as pH, scan rates, and 2,4-DNP concentration on the sensing capabilities of Cu_3BiS_3 catalysts. As depicted in Fig. 7a–c with varying concentrations, the

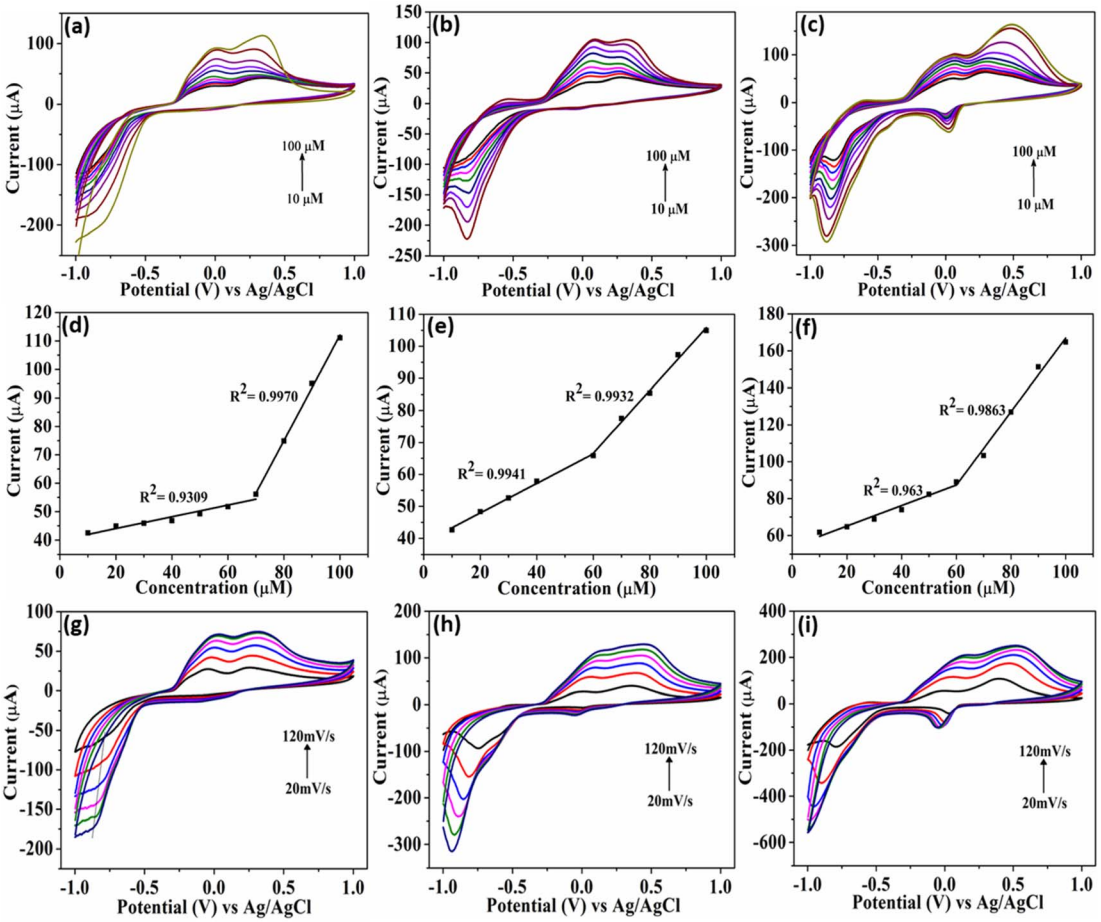

Fig. 6 CV of Cu_3BiS_3 at different concentrations of 4-NP (10–100 μm). (a) Cu_3BiS_3-DBU spheres, (b) Cu_3BiS_3-DABCO rods, and (c) Cu_3BiS_3-DBN worms. (d and e) The corresponding linear fit plots of current *vs.* concentration, and (g–i) CV at different scan rates of 20–120 mV s^{-1} of the three morphologies respectively.

Table 1 The LOD and sensitivity of Cu_3BiS_3 nanomaterials in detection of 4-NP and 2,4-DNP

Material	Experiment	LOD (μM)	LOQ (μM)	Sensitivity (μA μM^{-1} cm^{-2})
Cu_3BiS_3-sphere	4-NP	0.193	0.586	7.87
Cu_3BiS_3-rod	4-NP	0.135	0.410	13.87
Cu_3BiS_3-worm	**4-NP**	**0.103**	**0.314**	**26.23**
Cu_3BiS_3-sphere	2,4-DNP	0.158	0.480	0.087
Cu_3BiS_3-rod	2,4-DNP	0.110	0.333	0.082
Cu_3BiS_3-worm	**2,4-DNP**	**0.104**	**0.240**	**0.766**

reduction current increases with the rise in 2,4-DNP concentration, which is further evidenced by linear plots (Fig. 7d–f) illustrating the relationship between current and concentrations. Similarly, the influence of pH and scan rates was also investigated with the other parameters (Fig. S7 and S8†). The values of LOD, LOQ and sensitivity of the synthesized electrocatalysts are presented in Table 1. The findings reveal that the worm-shaped nanostructures exhibit the most effective sensing capability among the three different morphologies for detecting 2,4-DNP.

In addition, the electrochemical properties of Cu_3BiS_3 nanostructures were confirmed through chronoamperometry response for 4-nitrophenol (5–35 μm) and 2,4-dinitrophenol (10–50 μm) in a 20 ml solution at pH 6 PBS, under a potential of 0.30 V (Fig. 8a–f). The research indicated that the catalysts operational conditions were directly impacted by the regular addition of the substrates at 50 seconds intervals. Each incremental addition (5 μm for 4-nitrophenol and 10 μm for 2,4-dinitrophenol) displayed a consistent linear trend. The electrode system exhibited rapid responses to each 4-nitrophenol and 2,4-dinitrophenol addition and reached current saturation within 5 seconds. The linear correlation between current and concentration maintained a consistent pattern, demonstrating a proportional relationship between the response current and the concentrations of 4-nitrophenol and 2,4-dinitrophenol (Fig. S9†). This study underscores the sensitivity and precision of Cu_3BiS_3 morphological structures in detecting 4-nitrophenol and 2,4-dinitrophenol.

3.4. Interference study of 4-NP and 2,4-DNP with Cu_3BiS_3

The interference studies of 4-NP and 2,4-DNP were conducted in the presence of other potential interferents that could hinder

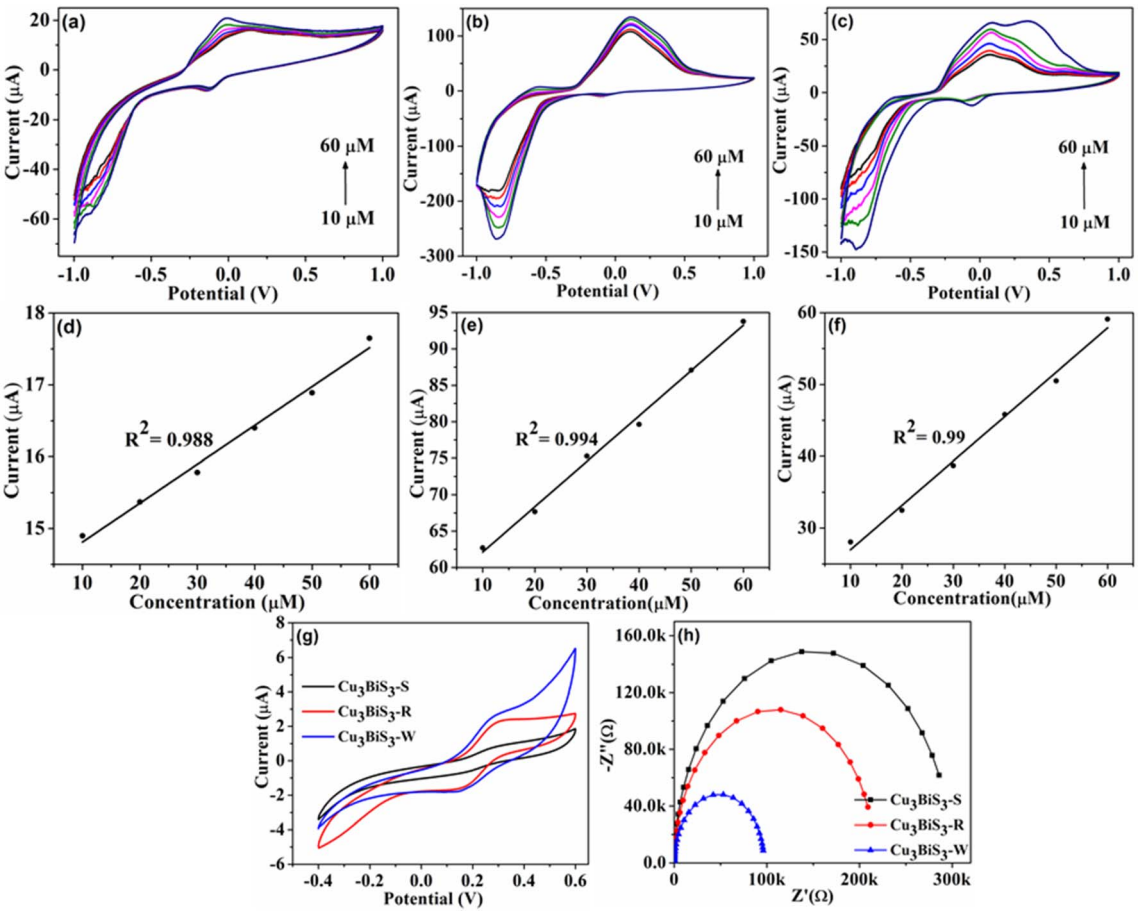

Fig. 7 (a–c) CV at different concentrations for 2,4-DNP, (d–f) linear plots of current *vs.* concentrations with three different morphologies. (g and h) CV and EIS plots of catalysts in 5 mM $K_3[Fe(CN)_6]$ with 0.1 M KCl solution.

the accurate detection of 4-NP and 2,4-DNP (refer to Fig. S10†). A range of interferents, including nitrobenzene, resorcinol, catechol, quinone, aniline, KCl, and acetate, were selected to demonstrate the selectivity of the modified electrode. It was observed that the Cu_3BiS_3 catalysts exhibited minimal change in current response in the presence of interferents when

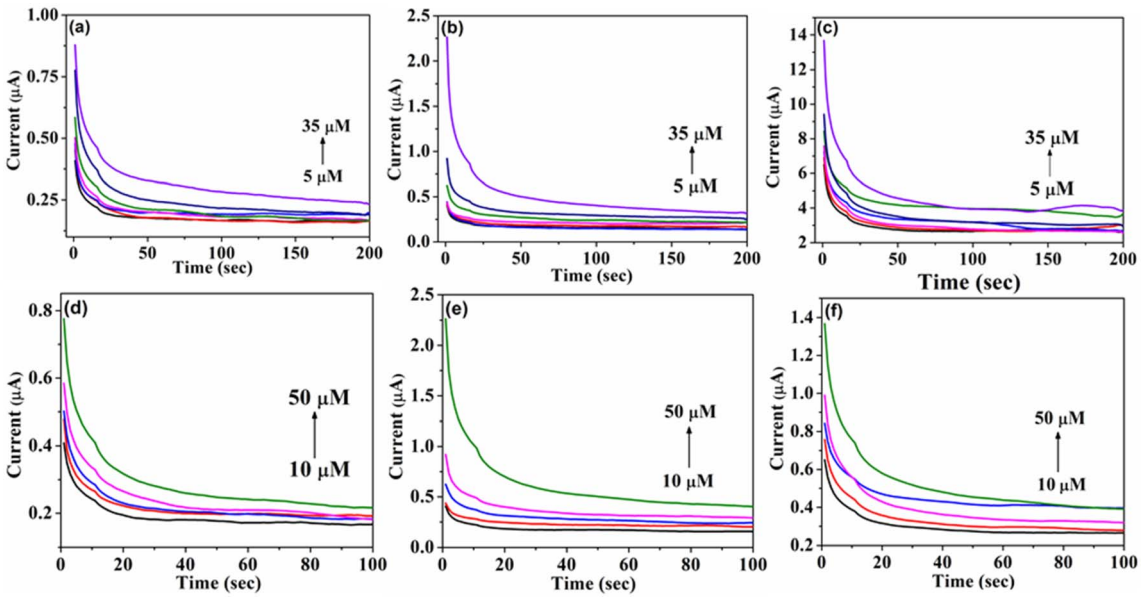

Fig. 8 Chronoamperometry studies of (a–c) 4-NP, and (d–f) 2,4-DNP for Cu_3BiS_3 spheres, rods, and worms respectively.

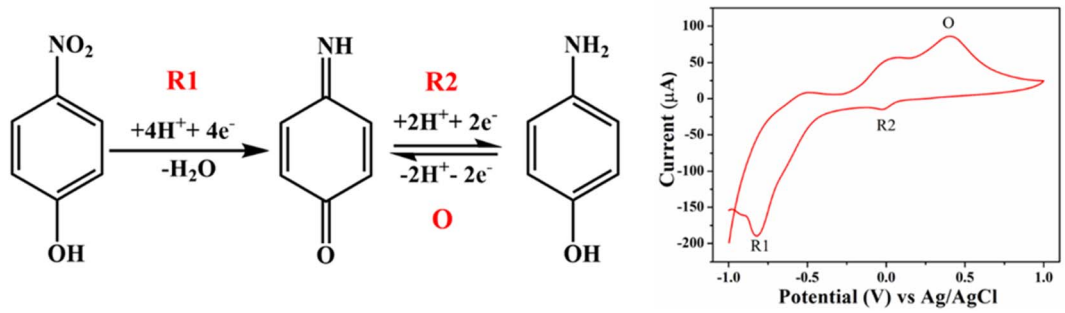

Fig. 9 Plausible detection mechanism of 4-NP and 2,4-DNP for three Cu_3BiS_3 catalysts.

compared to 4-NP and 2,4-DNP, even at higher concentrations. Among the three morphologies, the worm shape displayed exceptional *anti*-interference ability.

When Cu_3BiS_3 nanomaterial is used as an electrocatalyst to detect 4-NP, its mesoporous nanostructure can smoothen the adsorption of H_2O and 4-NP. Henceforward, 4-NP molecules can be electrochemically reduced to 4-hydroxylaminophenol (4-OH-AP) through the four-electron process (Step i), where the reduction peak (R1) is observed. Successively, the electrochemical oxidation–reduction interaction occurs between 4-OH-AP and 4-nitrosophenol *via* the two-electron process (Step ii), additionally ensuing in the predominance of the oxidation peak (O) and the other reduction peak (R2) (Fig. 9).[36] Likewise, the electrochemical detection of 2,4-DNP on the surface of Cu_3BiS_3 take place through the concurrent exchange of hydroxyl radical by removing two nitro groups (+0.031 and +0.32 V). The quinone is additionally reduced (−0.16, −0.58, and −0.80 V); hence, all the nitro groups are concentrated in amine groups.[18,37]

4 Conclusion

Utilising hydrothermal approach, Cu_3BiS_3 nanostructure with three distinctive morphologies were created and used for the electrochemical detection of 4-NP and 2,4-DNP. The nanostructures showed outstanding performance in precisely detecting trace levels of 4-NP with a LOD of 0.103 μM for worms, as well as in the detection of 2,4-DNP with LOD of 0.104 μM for worms. Due to the hierarchical morphology, small particle size, associated with numerous exposed active sites, and fast charge transfer the Cu_3BiS_3 nanostructure showed exceptional detectivity of nitro compounds. Here, the specific morphology comprising nanorods, nanospheres, and nanoworms is the key feature of Cu_3BiS_3 to achieve outstanding electrocatalytic performance. The Cu_3BiS_3 material exhibited exceptional long-term stability, selectivity, and reproducibility of catalysts. Our findings showed that morphology is also influencing catalytic activity in addition to the surface area. The use of nitrogenous base (DBN, DBU, and DABCO) tuned morphology will provide insight into building novel multifunctional, with hierarchical distinctive morphologies nanomaterials for sensing and other catalytic activities.

Data availability

The data supporting this article have been included as part of the ESI.†

Author contributions

Manzoor Ahmad Pandit, Dasari Sai Hemanth Kumar, Mohan Varkolu – data curation, formal analysis, investigation, methodology, writing – original draft Krishnamurthi Muralidharan – conceptualization, supervision, funding acquisition, writing – review & editing.

Conflicts of interest

The authors declare no conflicts of interest.

Acknowledgements

Authors thank Institute of Eminence grant (no. UoH-IoE-RC3-21-043) of University of Hyderabad for project (KM) and fellowship (DSHK). The instrument support grant from the Department of Science and Technology, New Delhi, India (through FIST program) is gratefully acknowledged. MAP thanks to ACHREM, University of Hyderabad for fellowship.

References

1 B. Srinivas, P. Manzoor Ahmad and K. Muralidharan, Importance of Clean Surfaces on the Catalyst: SnS_2 Nanorings for Environmental Remediation, *ACS Omega*, 2019, **4**, 14970–14980.
2 P. Manzoor Ahmad, B. Srinivas and K. Muralidharan, A simplistic approach for the synthesis of CuS-CdS heterostructure: A novel photo catalyst for oxidative dye degradation, *J. Environ. Chem. Eng.*, 2020, **8**, 103542.
3 P. Manzoor Ahmad, D. S. H. Kumar, B. Srinivas, M. Ramadoss and K. Muralidharan, Chalcopyrite with Magnetic and Dielectric Properties: An Introductory Catalyst for 4-Nitrophenol Reduction, *J. Phys. Chem. C*, 2020, **124**, 18010–18019.
4 A. Joseph, B. Srinivas, P. M. Ahmad, S. Khatun, A. K. Rengan and K. Muralidharan, Impact of bandgap tuning on ZnS for

degradation of environmental pollutants and disinfection. Environmental Science and Pollution Research, *Environ. Sci. Pollut. Res.*, 2022, **29**, 56863–56875.

5 G. A. Rather, A. Nanda and P. M. Ahmad, Green and Facile Synthesis of Zinc Oxide Nanoparticles Using Bergenia cilliata aqueous extract and evaluation of its photocatalytic activity, *J. Inorg. Chem. Comm.*, 2021, **134**, 109020.

6 P. M. Ahmad, D. S. H. Kumar, M. Ramadoss, Y. Chen and K. Muralidharan, Template free-synthesis of cobalt–iron chalcogenides [$Co_{0.8}Fe_{0.2}L_2$, L = S, Se] and their robust bifunctional electrocatalysis for the water splitting reaction and Cr(VI) reduction, *RSC Adv.*, 2022, **12**, 7762.

7 M. Ramadoss, Y. Chen, S. Zhe, M. Karpuraranjith, D. Yang, P. M. Ahmad and K. Muralidharan, Iron-Modulated 3D CoNiP Vertical Nanoarrays: An Exploratory Binder-Free Electrocatalyst for Efficient Overall Water Splitting, *J. Phys. Chem. C*, 2021, **125**, 20972–20979.

8 N. I. Ikhsan, P. Rameshkumar and N. H. Huang, Controlled synthesis of reduced graphene oxide supported silver nanoparticles for selective and sensitive electrochemical detection of 4-nitrophenol, *Electrochim. Acta*, 2016, **192**, 392–399.

9 K.-Y. Hwa, K.-Y. Ganguly, A. Santhan and T. S. K. Sharma, Synthesis of Water-Soluble Cadmium Selenide/Zinc Sulfide Quantum Dots on Functionalized Multiwalled Carbon Nanotubes for Efficient Covalent Synergism in Determining Environmental Hazardous Phenolic Compounds, *ACS Sustainable Chem. Eng.*, 2022, **10**, 1298–1315.

10 P. Wang, J. Xiao, A. Liao, P. Li, M. Guo and Y. Xia, Electrochemical determination of 4-nitrophenol using uniform nanoparticle film electrode of glass carbon fabricated facilely by square wave potential pulses, *Electrochim. Acta*, 2015, **176**, 448.

11 C. Rajkumar, P. Veerakumar, S.-M. Chen, B. Thirumalraj and K.-C. Lin, Ultrathin Sulfur-Doped Graphitic Carbon Nitride Nanosheets as Metal-Free Catalyst for Electrochemical Sensing and Catalytic Removal of 4-Nitrophenol, *ACS Sustain. Chem. Eng.*, 2018, **6**, 6021–16031.

12 Y. Yang, K. Jiang, J. Guo, J. Li, X. Peng, B. Hong, X. Wang and H. Ge, Facile fabrication of Au/Fe_3O_4 nanocomposites as excellent nanocatalyst for ultrafast recyclable reduction of 4-nitropheol, *Chem. Eng. J.*, 2019, **381**, 122596.

13 B. Wang, X. Lv, D. Feng, L. Xie, J. Zhang, M. Li, Y. Xie, J. Li and H. Zhou, Highly stable Zr(IV)-based metal-organic frameworks for the detection and removal of antibiotics and organic explosives in water, *J. Am. Chem. Soc.*, 2016, **138**, 6204–6216.

14 J. Zhang, T. Yao, H. Zhang, X. Zhang and J. Wu, Preparation of raspberry-like gamma-Fe_2O_3/crackled nitrogen-doped carbon capsules and their application as supports to improve catalytic activity, *Nanoscale*, 2016, **8**, 18693–18702.

15 S. Vinoth, P. Sampathkumar, K. Giribabu and A. Pandikumar, Ultrasonically assisted synthesis of barium stannate incorporated graphitic carbon nitride nanocomposite and its analytical performance in electrochemical sensing of 4-nitrophenol, *Ultrason. Sonochem.*, 2020, **62**, 104855.

16 Q. Ding, Z. Kang, L. Cao, M. Lin, H. Lin and D.-P. Yang, Conversion of waste eggshell into difunctional Au/$CaCO_3$ nanocomposite for 4-Nitrophenol electrochemical detection and catalytic reduction, *Appl. Surf. Sci.*, 2020, **510**, 145526.

17 L. Wang, T. Meng, G. Yu, S. Wu, J. Sun, H. Jia, H. Wang, X. Yang and Y. Zhang, A label free electrochemical biosensor for ultra-sensitively detecting telomerase activity based on the enhanced catalytic currents of acetaminophen catalyzed by Au nanorods, *Biosens. Bioelectron.*, 2019, **124–125**, 53–58.

18 T. Dhanasekaran, R. Manigandan, A. Padmanaban, R. Suresh, K. Giribabu and V. Narayanan, Fabrication of Ag@Co-Al Layered Double Hydroxides Reinforced poly(o-phenylenediamine) Nanohybrid for Efcient Electrochemical Detection of 4-Nitrophenol, 2,4-Dinitrophenol and Uric acid at Nano Molar Level, *Sci. Rep.*, 2019, **9**, 13250.

19 D. Chauhan, Pooja, V. Nirbhaya, C. Srivastava, R. Chandra and S. Kumar, Nanostructured transition metal chalcogenide embedded on reduced graphene oxide based highly efficient biosensor for cardiovascular disease detection, *Microchem. J.*, 2020, **155**, 104697.

20 S. Zhao, K. Wang, X. Zou, L. Gan, H. Du, C. Xu, F. Kang, W. Duan and J. Li, Group VB transition metal dichalcogenides for oxygen reduction reaction and strain-enhanced activity governed by p-orbital electrons of chalcogen, *Nano Res.*, 2019, **12**, 925–930.

21 E. Singh, K. Kim, G. Yeom and H. Nalwa, Two-dimensional transition metal dichalcogenide based counter electrodes for dye-sensitized solar cells, *RSC Adv.*, 2017, **7**, 28234–28249.

22 J. Cherusseri, N. Choudhary, K. Kumar, Y. Jung and J. Thomas, Recent trends in transition metal dichalcogenide based supercapacitor electrodes, *Nanoscale Horiz.*, 2019, **4**, 840–858.

23 J. Feng, X. Sun, C. Wu, L. Peng, C. Lin, S. Hu and J. Yang, Metallic few-layered VS_2 ultrathin Nanosheets: high two-dimensional conductivity for in-plane supercapacitors, *J. Am. Chem. Soc.*, 2011, **133**, 17832–17838.

24 B. Poudel, Q. Hao, Y. Ma, Y. Lan, A. Minnich, B. Yu, X. Yan, M. Dresselhaus, G. Chen and Z. Ren, High-Thermoelectric performance of nanostructured bismuth antimony telluride bulk alloys, *Science*, 2008, **320**, 634–638.

25 Q. Li, N. Zhang, Y. Yang, G. Wang and D. Ng, High efficiency photocatalysis for pollutant degradation with MoS_2/C_3N_4 heterostructures, *Langmuir*, 2014, **30**, 4–11.

26 G. Lee, S. Anandan, S. Masten and J. Wu, Photocatalytic hydrogen evolution from water splitting using Cu doped ZnS microspheres under visible light irradiation, *Renewable Energy*, 2016, **89**, 18–26.

27 Y. Zhang, Q. Zhou, J. Zhu, Q. Yan, S. Dou and W. Sun, Nanostructured metal chalcogenides for energy storage and electrocatalysis, *Adv. Funct. Mater.*, 2017, **27**, 1–34.

28 J. Li, Y. Zhao, X. Han and D. Xiao, A facile strategy for fabricating particle-on-flower Au-Cu_3BiS_3 nanostructures for enhanced photoelectrocatalytic activity in water splitting, *New J. Chem.*, 2021, **45**, 1231–1239.

29 N. Gerein and J. Haber, One–step synthesis and optical and electrical properties of thin film Cu_3BiS_3 for use as a solar absorber in photovoltaic devices, *Chem. Mater.*, 2006, **18**, 6297–6302.
30 F. Mesa, G. Gordillo, T. Dittrich, K. Ellmer, R. Baier and S. Sadewasser, Transient surface photovoltage of P-type Cu_3BiS_3, *Appl. Phys. Lett.*, 2010, **96**, 082113.
31 J. Li, X. Han, M. Wang, Y. Zhao and C. Dong, Fabrication and enhanced hydrogen evolution reaction performance of a Cu_3BiS_3 nanorods/TiO_2 heterojunction film, *New J. Chem.*, 2018, **42**, 4114–4120.
32 T. Manimozhi, J. Archana and K. Ramamurthi, Shape Controlled synthesis of Cu_3BiS_3 Nano-and microstructures by PEG assisted solvothermal method and functional properties, *Ceram. Int.*, 2018, **44**, 15385–15392.
33 P. Wang, J. Xiao, A. Liao, P. Li, M. Guo, Y. Xia, Z. Li, X. Jiang and W. Huang, Electrochemical determination of 4-nitrophenol using uniform nanoparticle film electrode of glass carbon fabricated facilely by square wave potential pulses, *Electrochim. Acta*, 2015, **176**, 448–455.
34 P. Balasubramanian, T. Balamurugan, S.-M. Chen and T.-W. Chen, Simplistic synthesis of ultrafine $CoMnO_3$ nanosheets: An excellent electrocatalyst for highly sensitive detection of toxic 4-nitrophenol in environmental water samples, *J. Hazard. Mater.*, 2019, **361**, 123–133.
35 S. Ramki, R. Sukanya, S.-M. Chen, M. Sakthivel and J. Wang, Simple hydrothermal synthesis of defective $CeMoSe_2$ dendrites as an effective electrocatalyst for the electrochemical sensing of 4-nitrophenol in water samples, *New J. Chem.*, 2019, **43**, 17200.
36 M. Wang, Y. Liu, L. He, Z. Zhang, Q. Jia, Y. Song and S. Fang, Bimetallic metal–organic framework derived FeOx/TiO_2 embedded in mesoporous carbon nanocomposite for the sensitive electrochemical detection of 4-nitrophenol, *Sens. Actuators, B*, 2019, **281**, 1063–1072.
37 S. Md Abdus, C. S. Pallab, M. R. Mohammed, A. Jahir, M. A. Abdullah and Al-M. Mohammad, Fabrication of a 2,4-dinitrophenol sensor based on Fe_3O_4@Ag@Ni nanomaterials and studies on their antibacterial properties, *New J. Chem.*, 2018, **42**, 872–881.